A Cerium-Based Nanocoating for Corrosion Protection of the AA1230 as Clad Material for the AA2024-T3 Alloy

*Rafael Emil Klumpp[a]** ⓘ*, *João V. de S. Araujo[a]* ⓘ, *Renato Altobelli Antunes[b]* ⓘ,

Bárbara Victoria Gonçalves de Viveiros[a] ⓘ , *Marina Magnani[c]* ⓘ, *Isolda Costa[a]* ⓘ

[a]Instituto de Pesquisas Energéticas e Nucleares, Av. Prof. Lineu Prestes, 2242, SP, Brasil.
[b]Universidade Federal do ABC (UFABC), Centro de Engenharia, Modelagem e Ciências Sociais Aplicadas (CECS), 09210-580, Santo André, SP, Brasil.
[c]Universidade Estadual Paulista Júlio de Mesquita Filho (Unesp), Instituto de Química (IQ– Campus Araraquara), 14800-060, Rua Prof. Francisco Degni, 55 - Quitandinha – Araraquara, SP, Brasil

Aluminum alloys are the state-of-art materials for structural components of aircrafts. As they are susceptible to localized corrosion, this kind of damage can become a major threat for its safe use in aircraft components. Therefore, surface protection of aluminum alloys against corrosion is a core issue in these applications. In this work, an alternative eco-friendly cerium-based surface pretreatment was developed and applied on the AA1230 clad of the AA2024-T3 alloy for corrosion protection. The corrosion resistance evaluation of this modified surface was evaluated by several techniques. The results were compared to chromium based conventional treatments and revealed that the coating layer, composed of spherical nodular nanostructures of cerium, obtained with the proposed eco-friendly treatment, improved the corrosion resistance of the alloy. Moreover, it was comparable to the corrosion behavior of chromate-treated alloy, showing that this treatment is a promising alternative to replace chromate based surface treatments.

Keywords: *AA1230; Surface treatment; Corrosion; Clad 2024.*

1. Introduction

Aluminum alloys have been extensively employed in the structure of commercial and military aircrafts due to their low-density combined with high mechanical strength. The low density of these alloys is an important factor for their application as structural materials in the aircraft industry due to the high impact of weight reduction on fuel consumption[1-3] Also, the improvement of mechanical properties influences operating costs, since the time interval between maintenances can be increased. Besides their good mechanical properties, these alloys present high susceptibility to localized corrosion due to microstructural heterogeneities such as precipitates that contribute to alloy strengthening, but increase the tendency to localized attack due to micro galvanic effects[4-6]. In order to improve the corrosion resistance of Al alloys the use of protective coatings on the alloys surface has been largely adopted. Common practice in the aircraft industry is the use of cladding and/or anodizing of Al alloys[7]. For aircraft aluminum structural parts where corrosion resistance is essential and deterioration of mechanical properties due to the anodizing process is of concern cladding represents a well-established solution[3]. Structural parts of aircrafts made of Al alloys that are exposed to corrosive environments are either cladded with a layer of commercially pure aluminium (clad) covering their surfaces or anodized. The clad layer (commercially pure Al) is more resistant to localized corrosion than the substrate (AA2024-T3). However, the clad material is not immune to corrosion and its protection is usually carried out by surface treatments such as conversion coatings, but not anodizing. In the AA2024-T3 alloy, the S phase is the main responsible for localized corrosion attack, besides Fe-rich particles, which are sites for oxygen reduction reaction, and promote the nucleation of corrosion pits[3,7,8]. The AA2024 alloys for exposure to environment corrosive solutions are usually anodized and coated with paints.

Surface treatments that produce conversion layers from solutions containing hexavalent chromium have been widely used and are highly effective for protecting aluminum alloys against corrosion. However, the waste generated from these treatments are extremely harmful to health (mutagenic) and environment (toxic and carcinogenic). Concerns about environment and health have increasingly restricted the use of these chromium-based treatments. Alternatives to solve this problem are related to the development of substitute treatments that do not generate toxic residues and promote corrosion resistance similar to those obtained by chromate conversion layers[1-3]. In this sense, rare earth-based conversion treatments have proved highly promising to replace conventional treatments based on hexavalent chromium[1,2,9,10]. This is due to the characteristics of lanthanide ions, such as Ce^{3+}, Y^{3+}, La^{3+}, Pr^{3+}, Nd^{3+}, which form insoluble hydroxides that passivate

*e-mail: rafahemil@hotmail.com

the surface, acting as corrosion inhibitors for aluminum, besides having low toxicity[7,8]. Literature reports[9,11] that the self-healing characteristic of these cerium conversion coating layers is due to the existence of metastable species of Ce in the substrate-coating interface. These metastable species would be able to interact with Al^{3+} generated by the alloy during corrosion process, forming Ce-Al-O phases.

The search for alternative treatments that promote corrosion resistance similar to those obtained by layers of conversion with hexavalent chromium has been the subject of a large number of researches in recent decades, and the object of study of this work is to propose an eco-friendly alternative based on a cerium based nanocoating.

2. Experimental

The substrate used in this study was an AA2024-T3 alloy cladded with AA1230. The AA1230 (Al 99.3%, Si+Fe 0.7%, Cu 0.1%, Mn 0.05%, Mg 0.05%) cladding layer present on both sides present thickness in the range of 60–80 μm. The clad layer is not removed by the surface treatments to which it was subjected. Samples of the cladded alloy had their surfaces firstly prepared by degreasing in ethanol. Three different sets of samples were produced. Details of each condition and pretreatment are presented next. The first set of samples, designated as CeHT, was treated by immersion in a solution composed of 0.01 mol L^{-1} hydrated $Ce(NO_3)_3$ at 4.5 pH. The immersion treatment was carried out for 7 min at 70 °C and then, the samples were rinsed with DI water followed by drying in an oven at 105 °C for 10 min. This concentration, time and temperature was based in previous work carried out in our laboratory[12,13]. The second set of samples, designated as CrVI, was treated by immersion in a commercial chromate bath (Alodine 1000) for 3 min at room temperature and then, rinsed with DI water (according Alodine 1000 Technical Data Sheet) followed by drying in an oven at 105 °C for 10 min[14,15]. The third set was used as a control, being designated as Control that corresponded to samples without any conversion layers, degreased in ethanol and dried in an oven at 105 °C for 10 min.

Electrochemical tests were conducted in 0.1 mol L^{-1} NaCl solution using a Gamry potentiostat PCI4/300. The 0.1 mol L^{-1} saline solution concentration was chosen after preliminary tests carried out that indicated this concentration was proper to monitor corrosion evolution at the surface of the cladded alloy. The solution that simulates the composition of sea water (0.6 mol L^{-1} NaCl) was too aggressive to the tested material leading to intense localized attack. This solution has been used also because it is not too mild to lead to slow kinetics that would demand long periods of monitoring. Potentiodynamic polarization tests were carried out in the sequence of EIS at the same area tested by EIS with the aim of obtaining kinetic information of the tested material from the same exposed area.

A three-electrode set up comprised of the sample as working electrode, a Pt counter electrode and an Ag/AgCl (saturated KCl) reference electrode, was used for the experiments. Electrochemical Impedance Spectroscopy (EIS) tests were carried out after 24 h and 48 h of immersion, from 50 kHz to 10 mHz, with an amplitude of perturbation of 10 mV (rms) and at an acquision rate of 10 points per frequency decade. Potentiodynamic polarization curves were obtained in 0.1 mol L^{-1} NaCl solution at (23 ± 2) °C. Anodic

polarization tests were carried out from -0.03 V (vs OCP) to 1 V (vs $E_{Ag/AgCl (KCl sat)}$). The polarization curves were obtained after 24 hours of immersion using a scan rate of 0.5 mV s^{-1}.

Scanning electron microscopy (SEM) was performed using a JEOL JSM 6010 microscope equipped with an energy dispersive X-ray spectroscopy (EDS) detector.

All samples were evaluated by scanning vibrating electrode technique (SVET) using an Applicable Electronics™ SVET machine controlled by an Automated Scanning Electrode Technique (ASET 4.0) software. An insulated Pt–Ir probe was used as the vibrating electrode for the SVET system. A 15 μm diameter platinum sphere was electrodeposited at the tip of the probes prior to start SVET tests. The amplitude of vibration was 19 μm, and the vibrating frequencies of the probe were 174 Hz (X) and 73 Hz (Z). 35 × 25 points were obtained for each SVET map. The time lag between each current density data-point acquired was 0.5 s, and the scan step interval was 200 μm. All experiments were performed in a Faraday cage at (20 ± 2) °C. The 5x5 mm samples used as working electrodes were embedded in epoxy resin. Experiments were performed in 0.005 mol L^{-1} NaCl for 24 h and SVET maps were obtained every 2 h.

X-ray photoelectron spectroscopy analysis (XPS) of the treated surfaces was carried out using a ThermoFisher Scientific K-alpha+ spectrometer operating with a monochromated Al-Kα radiation source (1486.6 eV) and a spot size of 400 μm to obtain the maximum signal over the largest possible area. High-resolution spectra were obtained using pass energy of 50 eV. Peak fitting was performed using a mixture of Gaussian-Lorentzian functions in the Vantage™ software with background subtraction by the Smart algorithm. Binding energy scale was calibrated by referencing the C1s value at 248.8 eV.

Atomic Force Microscopy (AFM) experiments were performed using an Agilent AFM system Model 5500 equipment (Agilent Technologies, Chandler, AZ, USA) in tapping mode and at room temperature using a probe with long cantilever and aluminum reflective coating. Typical settings adopted were tip thickness 7 μm, cantilever length 225 μm, width 38 μm, force constant 48 Nm^{-1} and resonant frequency 190 kHz (TAP 190AL-G budget sensors) and the loading velocity of tip was 0.55 ln/s. The 3D topography images were obtained using Gwyddion software.

Contact angle experiments were performed using a Thermo Cahn DCA 300 equipment, with WinDCA 300 software with the analysis being based on the Wilhelmy plate method[16].

Neutral Salt Spray Testing (NSST) experiments were performed according to ASTM B117[31]. The samples were treated as described earlier and received an epoxy colorless coating (35 microns) to simulate the painted surface to the substrate. The performance of the modified surface with defects induced by scratches carried out by inducing X-cut incision to simulate a mechanical defect, according to ASTM D3359[17], was also evaluated.

3. Results

3.1. Electrochemical evaluation

EIS results of the CeHT treated and Control samples obtained after 24 h and 48 h of exposure are compared in Figure 1. In Figure 1 two-time constants are suggested for both surfaces, Control and CeHT, regardless of the exposure

time which were identified by a flattened arc from high to medium frequencies followed by a tail at low frequencies in the Nyquist plots. In the Bode phase angle plots, the two-time constants are indicated by the two peaks seen in the graphs corresponding to the Control samples, whereas for the CeHT surfaces two overlapped or partially overlapped time constants could be identified. Electrical equivalent circuits (EECs) were not used in this study once there are many criticisms to the use of EECs to simulate the interface between the exposed material and the corrosive environment without the use of other techniques of characterization of the surface. Different EECs might result in good fitting to the experimental data and, consequently, the use of EECs to obtain information on the interface between the material exposed and the environment should not be used without the use of supplementary characterization techniques.

The capacitive behavior related to the CeHT samples indicates the presence of a passive layer on the surface. Comparatively, the CeHT presents higher impedances compared to the Control one. Figure 1B shows shifting of the phase angle to lower frequency regions for CeHT samples probably due to hydration of the oxide layer that increases the surface resistance.

Figure 2 compares the EIS results of the three surface conditions evaluated in this work after 24 h of exposure to the test solution. The CrVI condition presented the highest impedances due to a 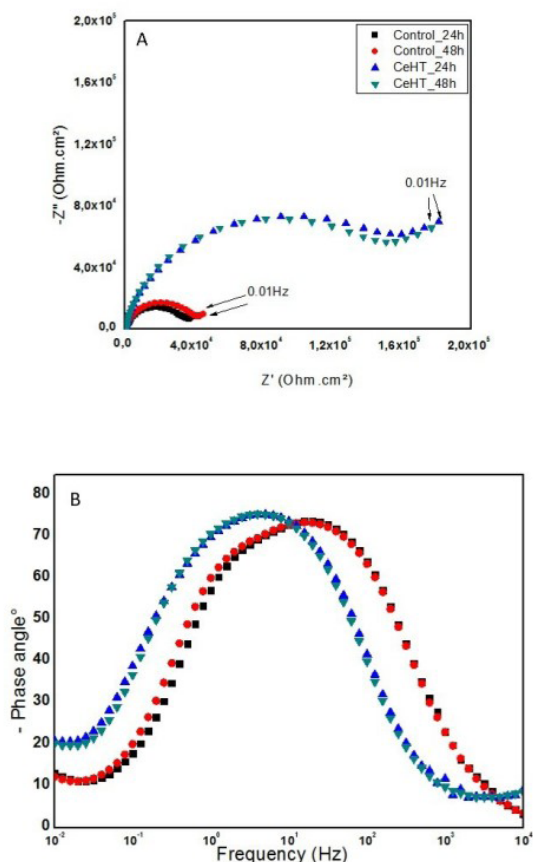coating layer composed of Cr_2O_3 that serves as a barrier to corrosion acting as cathodic and anodic inhibitor[13,14]. Despite the higher impedances related to the CrVI condition, the CeHT treatment resulted in significant increase in impedance comparatively to the untreated (Control) samples and a surface that presents high stability, as shown in Figure 1. The literature[2,11,18,19] reports remarkable corrosion resistance for chromated aluminum surfaces and despite the great number of research studies carried out along the last decades, a single step surface treatment that results in corrosion resistance similar to that produced by chromating treatments has not yet been found. Due to this, single step surface treatments that lead to improved corrosion resistance and surface stability are of great interest.

The anodic polarization curves, Figure 3, show similar behavior for the Control and CeHT samples, with slightly current densities associated to the CeHT sufaces. The curves show that at the corrosion potential the current densities for all samples are typical of passive materials with values of 10^{-9} and 10^{-8} A/cm^2 for the Control and CeHT samples, respectively, and 10^{-7} A/cm^2 for the CrVI samples. The results show that all surfaces are passive at the corrosion potential. The CrVI treatment resulted in nobler corrosion potentials, but also in depolarized anodic reactions. This means that at low overpotentials the corrosion current densities will largely
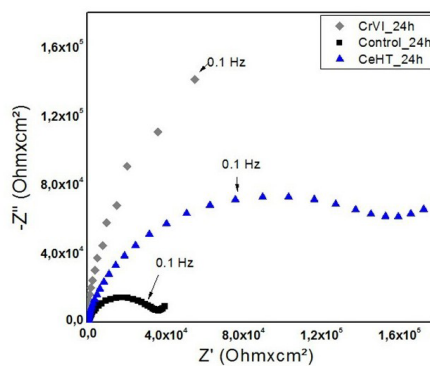

Figure 2. Comparative Nyquist plots for AA1230 clad on AA2024 alloy with various pre-treatments after 24 h of exposure to 0.1 mol L^{-1} NaCl solution.
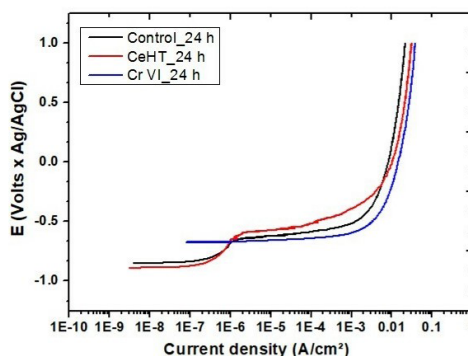

Figure 1. EIS results for AA1230 clad on AA2024 alloy with various pre-treatments after 24 h and 48 h in 0.1 mol L^{-1} NaCl solution.

Figure 3. Anodic polarization curves for AA1230 clad on AA2024 alloy with various pre-treatments after 24 h in 0.1 mol L^{-1} NaCl solution at (23 ± 2) °C and at a scan rate of 0.5 mV s^{-1}.

increase showing fast kinetics of the anodic reactions. The CeHT surface presented a breakdown potential of approximately -0.58V whereas that of the Control sample was nearly -0.67 V, showing that the CeHT treatment improved the resistance of the surface film to breakdown. The growth of the hydrated layer and the incorporation of Ce in it results in inhibition of the corrosion process by improving the resistance of the surface layer to film breakdown.

SVET technique has been used to study the corrosion phenomena by measuring the local ionic currents by many researches[6,20]. The development of localized attack was monitored by SVET during exposure to 0.005 mol L^{-1} NaCl solution (Figure 4). In the SVET maps, red represents anodic activity, while blue represents cathodic activity, as indicated by the current density scale[6]. During the whole test, the Control surface presented higher anodic current densities compared to the two other conditions, as expected. Also, it was observed that the current density reduced with the exposure time to the test solution. This result is associated with the healing effects associated to the layer formed during the surface treatment. The self-healing effects of CrVI treatment is very well-known, recently, many researches have been directed to the self-healing effect of Ce ions impregnated in surface film[21-24]. A comparison of SVET maps related to the CeHT and CrVI surfaces, showed lower electrochemical activity related to the CeHT compared to the CrVI surface. For the CrVI surface, the self-healing effect is clearly identified in the SVET maps, corresponding to 2 h and 12 h, where a clear spot of localized corrosion seen at 2 h (indicated by an arrow) is not observed at 12 h. For the CeHT surface there was also evidence of decreased electrochemical activity between 12 h and 24 h at some areas

of the surface. The SVET maps for CeHT suggested lower anodic activity compared to the CrVI at all times and the currents were also more homogeneously distributed on the CeHT surface. A comparison of the anodic currents for the CeHT and CrVI treated surfaces are shown in Figure 5 as 3D SVET maps for 6 h exposure to the test solution. The results in Figure 5 support the improved distribution of anodic currents related on the CeHT surface compared to the CrVI surface, indicating a better corrosion protection associated to the surface layer produced by the CeHT.

3.2. Morphological characterization

Figure 6 compares the morphologies of the Control and the CeHT treated surfaces by means of SEM micrographs. At low magnifications it is not possible to observe differences on the surface morphology. However, at high magnifications a clear distinction between the CeHT treated surface and the Control one is seen. The surface layer corresponding to the CeHT sample is formed by spherical nodular nanostructures with diameters lower than 100 nm, while the surface of the Control sample presents only the characteristics of the cladded alloy showing precipitates (white particles) and scratches resulting from the material's fabrication.

AFM results shown in Figure 7 clearly distinguish the differences in the morphology of the surface related to the Control and CeHT samples. For this last type of surface, spherical nodular nanostructures cover the treated surface showing the morphology of the cerium-based film. The spherical structures covered the surface and reach a maximum height of about 67 nm. The CeHT treated surface was covered and the surface roughness decreased, as indicated in Figures 7C Control and 7(D) CeHT. Hydrothermal treatments lead to
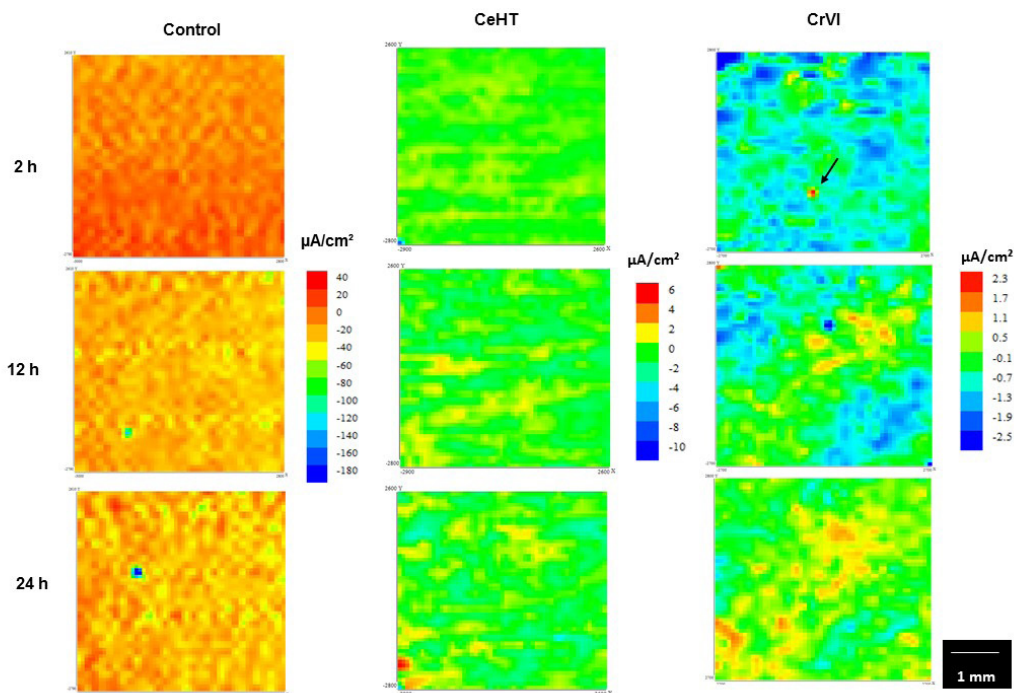

Figure 4. SVET maps obtained for AA1230 clad on AA2024 alloy with various pre-treatments (Control, CeHT and Cr VI) Measurements taken after exposure in NaCl 0.05 mol L^{-1} for 2 h, 12 h and 24 h.
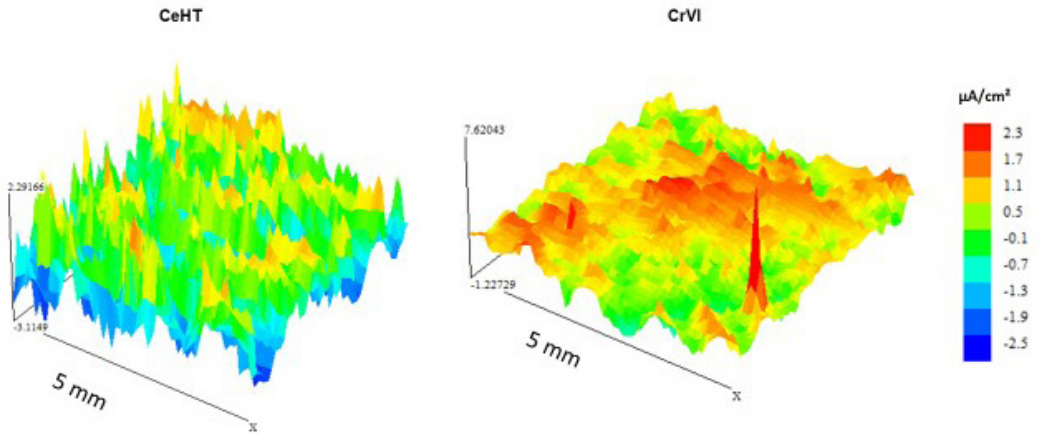
Figure 5. 3D SVET maps obtained for AA1230 clad on AA2024 alloy with various after CeHT and CrVI treatments. Measurements obtained after 6 h of exposure in NaCl 0.05 mol L^{-1}.
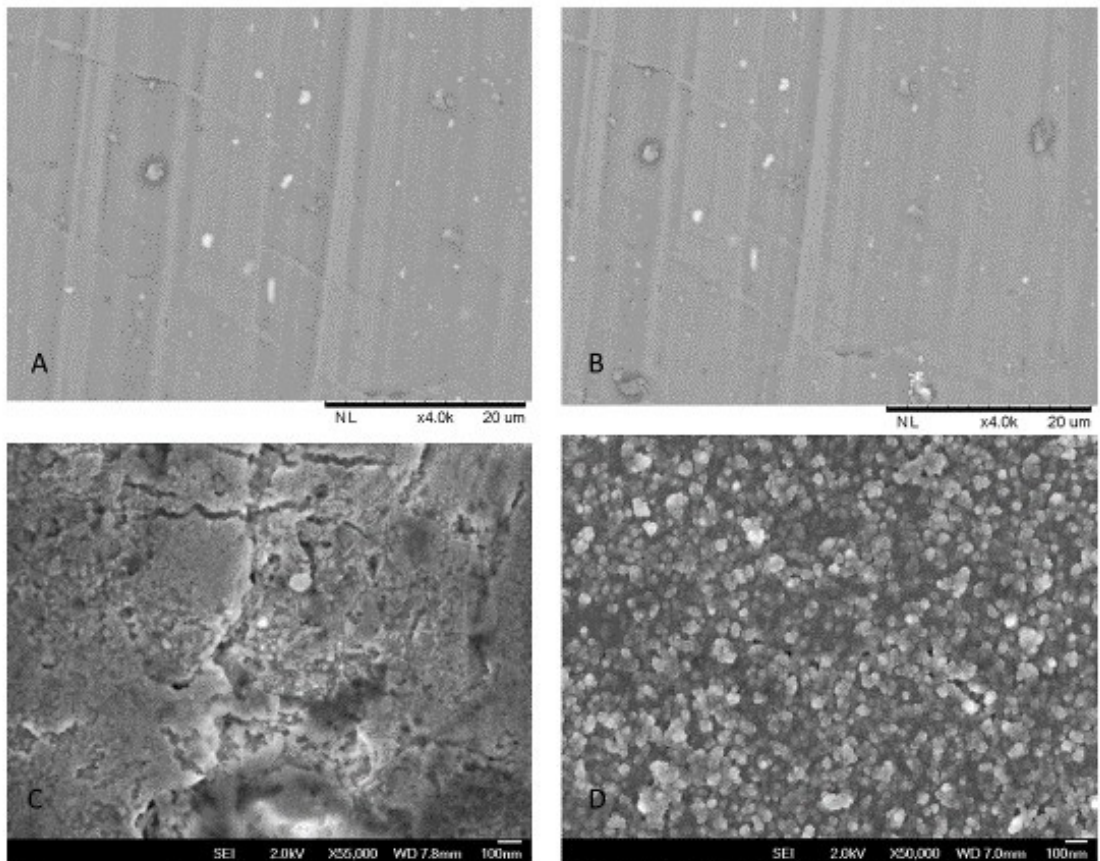

Figure 6. SEM micrographs showing (A) Control AA1230 clad on AA2024 alloy at low magnification, (B) same area after CeHT treatment, (C) Control AA1230 clad on AA2024 alloy at high magnification and, (D) CeHT treated surface at high magnification.

the formation of boehmite and pseudo-boehmite layer that consists of a combination of hydroxides and aluminum oxide layer (Al$_2$O$_3$ and Al(OH)$_3$). It is important to emphasize that the structure of boehmite/pseudo-boehmite is typically lamellar[16,18,19]. Therefore, the nodular structure associated to the CeHT surface suggests the effect of interaction of cerium

ions with the boehmite/pseudo-boehmite layer during the hydrothermal process.

The contact angle related to both surfaces was measured. The results show that the contact angle decreased for the CeHT treated surface, as displayed in Table 1. Hence, the CeHT treated surface presents higher hydrophilicity compared to
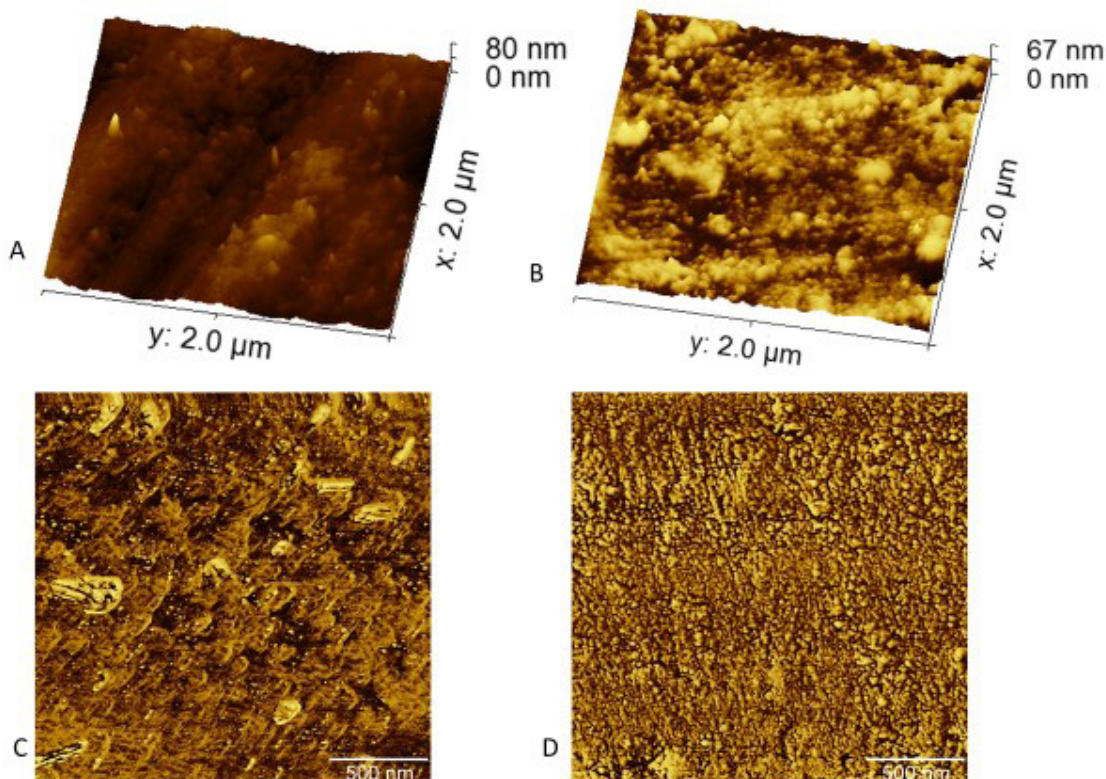
Figure 7. AFM micrographs of AA1230 clad on AA2024 alloy. (A) 3D of Control surface, (B) 3D CeHT treated surface. (C) 2D of Control surface (D) 2D of CeHT treated surface.

Table 1. Results of contact angle measurements.

Treatment	Contact angle (°)	Standard Deviation
Control	85.91	0.9987
CeHT	61.24	0.8619

Table 2. Results of EDS analysis for O, Al and Ce (weight %) of AA1230 clad treated with CeHT.

	O	Al	Ce
Pt 1	6.90%	83.93%	9.17%
Pt 2	6.18%	84.85%	8.97%

the Control surface. It is accepted that surfaces with water contact angle greater than 90 °C are hydrophobic[20]. The growth of pseudo-boehmite during the CeHT treatment explains the increased hydrophilic bonds available at the CeHT treated sample, providing a surface of improved wettability. This characteristic is useful for post-treatments where hydrophilic bonds are important for adhesion between layers[25].

3.3 Chemical composition characterization

Semi-quantitative composition analysis of the CeHT treated surface was carried out by EDS at two points at the surface and the results are presented in Table 2.

As expected, the EDS analysis showed that treatment produces a coating layer formed that have Al, O and Ce as main elements.

The chemical composition of the CeHT treated surface was also analyzed by XPS. The main elements were Al, O and Ce in accordance with the EDS analysis. The C 1s peak is related to common carbon contamination caused by contact with air, which is known as "adventitious carbon layer (AdC)",[26,27] The high-resolution Al 2p spectrum, Figure 8A,

showed a single component peak at a binding energy of ~74.3 eV, centered in the position of Al(III) compounds, which is consistent with the presence of Boehmite[28,29]. Also, the high-resolution O 1s spectrum, Figure 8B, shows that the highest intensity peak was centered at a binding energy of 532.14 eV which is attributed to Al hydroxide species[28,30]. The lower intensity of the peak centered at 530.9 eV is consistent with the presence of Al oxide species[28,30]. It is important to notice that cerium has also contribution in oxide and hydroxide species. The difference of intensity between the hydroxyl peak and the oxide peak, Figure 8B, indicates that the hydroxyl groups are the major component in the surface layer, according to a hydrated oxide surface[29] typical of pseudo-boehmite. The incorporation of water into the crystal structure leads to high intensity hydroxyl peaks[28,30]. The peak centered at 533.4 eV binding energy is due to absorbed water. The high-resolution Ce 3d spectrum[29], Figure 8C, is composed by two doublets peaks; the less intense, centered at nearly 905 eV and the most intense at approximately 885 eV. The characteristic peak for Ce^{4+}, at
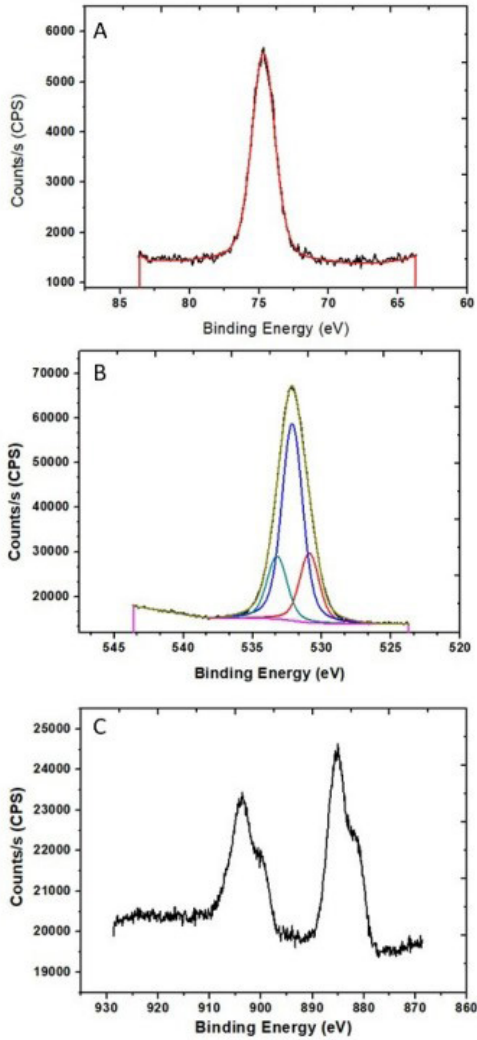
Figure 8. High-resolution spectra of CeHT treated surface of AA1230 clad on AA2024 alloy; where (A) Al 2p, (B) O 1s and (C) Ce 3d.

around 916 eV was not found, suggesting that the formed layer is mainly composed of Ce^{3+} present in the coating as oxide/hydroxide[28].

3.4. Accelerated neutral salt spray corrosion test (NSST)

The various types of surfaces tested with results presented in the previous sections were covered by an epoxy colorless coating (35 microns), to simulate a painted surface. The epoxy coated layer was scratched and the samples were tested by neutral salt spray tests carried out according to ASTM B117[31]. The results corresponding to 168 h of exposure to NSST are shown in Figure 9. The surface corresponding to the Control sample presented very poor corrosion resistance, as the surface was severely degraded, and is covered by pits and corrosion products after 168 h of exposure to NSST. In the scratched area, the presence of large amounts of corrosion products is

seen. The CeHT surface showed good corrosion resistance, comparable to that of the CrVI treated one.

4. Discussion

As indicated by SEM and AFM results, the CeHT treatment produces a coating layer formed by spherical nodular nanostructures with diameters lower than 100 nm. The EDS and XPS results showed that this coating is mainly formed by a hydrated oxide where Ce is incorporated. The results suggest that these spherical nodular nanostructures are a cerium modified pseudo-boehmite formed during the hydrothermal process. The coating starts being formed with the Al-O covalent bonds in the naturally formed film of Al_2O_3. The literature suggests that hydrothermal treatments in aluminum alloys results in pseudo-boehmite (OAlOH-HOAlO) and boehmite (AlOOH) films from Al_2O_3 and $Al(OH)_3$, formed together with aluminum oxy/hydroxides when exposed to aerated aqueous media[28,32]. Subsequently, the formation of aluminum oxy/hydroxides film occurs that results in surface alkalinization[33]

$$Al_2O_3 + 2OH^- + 3H_2O \; 2\left[Al(OH)_4\right]^- \tag{1}$$
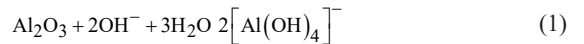
The alkalization resulting from the hydrothermal process leads to the formation of tetra aluminum hydroxide, Equation 1[34] The literature reports that Cerium, because of its coordination, when in nitrate containing solutions, has the ability to form complexes, such as ($[CeNO_3]^{2+}$ and $[Ce(NO_3)_2]^+$)[35,36]. These can be incorporated into the surface layer, and once they are positively charged, may react with aluminum tetrahydroxide, which are negatively charged. As indicated earlier, boehmite/pseudo-boehmite layer presents a lamellar structure[23,32], whereas the nodular structure shown for the CeHT treatment, suggests the interaction of cerium nitrate complex with the boehmite/pseudo-boehmite formed during the hydrothermal process. The literature reported the production of non-lamellar boehmites. He and Zhu[32] produced non-lamellar particles with a length of approximately 100 nanometers by hydrothermal treatment in a solution with nitrate and with pH 4. They ascribed the different morphology to pH and the electrostatic attraction between nitrate anion and boehmite surface[16]. Boehmite exhibits a lamellar structure with an orthorhombic symmetry whose layers consist of OAlOH-HOAlO oriented from the [100] to [001] directions. Adsorption of free nitrate to hydroxyl leads to the formation of $Al_2O_2(OH)NO_3$ causing the boehmite growth to be changed from [010] to [100]. The composition is in accordance with the contact angle results that showed good interaction of the formed layer with water, as pseudo-boehmite is generated by hydrogen bonding forming together with the layers of aluminum oxide and hydroxide. This kind of bonding has a strong interaction with water. This interaction was supported by the high degree of hydration presented in the XPS high resolution spectra.

The results from the accelerated corrosion tests were in accordance with the electrochemical ones, indicating good corrosion protection of the substrate. Thus, it is suggested that the hydrated oxide layer obtained from the CeHT treatment results in high corrosion resistance, comparable to that of
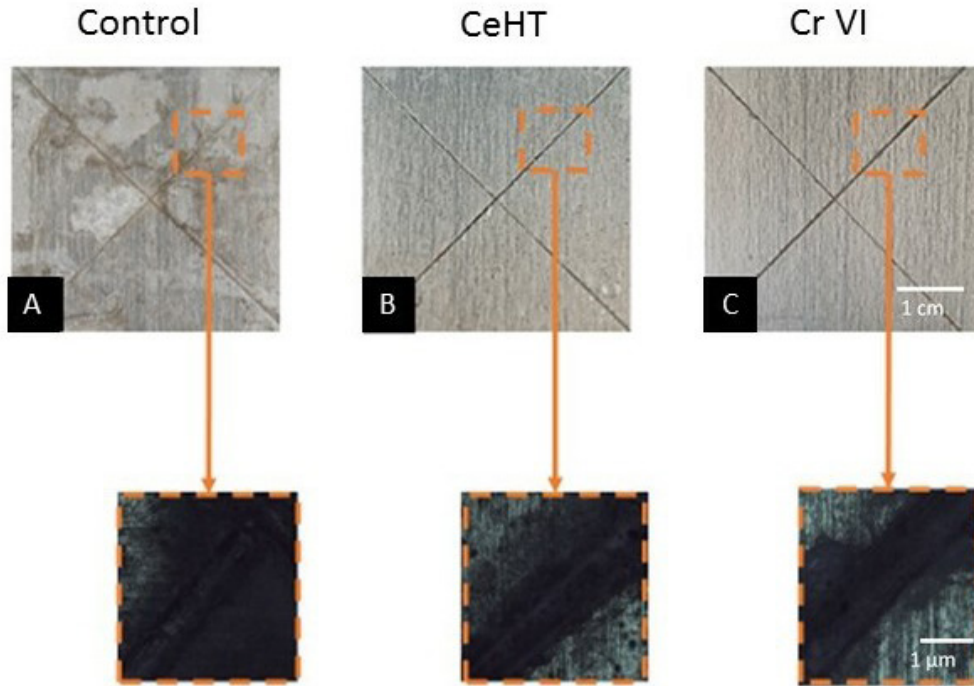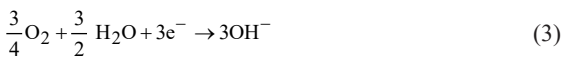
Figure 9. Visual aspect of samples of AA1230 clad on AA2024 alloy in the surface condition (A) Control, (B) CeHT treated NS (C) CrVI treated.

the CrVI treated surface. It might also suggest that the cerium-treated surface presents self-healing properties due to Ce^{3+} ions release at areas where anodic dissolution of the aluminum substrate has started (Equation 2), and blocking the layer defects, by precipitation of mixed Aluminum/Cerium Oxides, caused by oxygen reduction occurred at the cathodic sites with a pH increase (Equations 3 and 4). Many authors have been reported that cerium acts as a cathodic inhibitor, precipitating in the cathodic areas, suppressing the anodic reactions[1,12,15,37-39].

$$Al^\circ \rightarrow Al^{3+} + 3e^- \qquad (2)$$

$$\frac{3}{4}O_2 + \frac{3}{2}H_2O + 3e^- \rightarrow 3OH^- \qquad (3)$$

$$Ce^{3+} + 3OH^- \rightarrow Ce(OH)_3 \qquad (4)$$

There is evidence that Ce incorporated in surface coating layers has self-healing effects by precipitating at electroactive sites at the substrate. Another observation of this work is that the incorporation of Ce into the surface coating affects its morphology, and this can modify the coverage of the substrate and, consequently, the barrier effect of the coating formed. Those are different effects, but both interfere with the corrosion protection of the substrate.

Both treatments compared in this study, CeHT and CrVI, were obtained by one step treatment in a simple manner, that is, by immersion in aqueous solutions for a short period (few minutes) followed by drying in an oven. The main advantage of the CeHT treatment is that it does not

generate toxic residues thus does not produce harm either to the environment or to the human health.

5. Conclusions

The coating layer generated by a hydrothermal treatment in a cerium nitrate containing solution (CeHT) used in this study was found to be formed by spherical nodular nanostructures of a cerium modified pseudo-boehmite. The formed layer allows an uniform coverage of the whole surface providing good distribution of anodic currents at the surface and high corrosion resistance to the AA1230 clad on AA2024 alloy. The CeHT treatment resulted in comparable results to that produced by the CrVI treatment, either by electrochemical tests or accelerated neutral salt spray test. The results pointed out that hydrothermal treatments in the presence of Ce ions might be a proper alternative to replace the toxic carcinogenic chromating surface treatments for Al alloys.

6. References

1. Harvey TG. Cerium-based conversion coatings on aluminium alloys : a process review. Corros Eng Sci Technol. 2013;48(4):248-69.
2. Kulinich SA, Akhtar AS. On conversion coating treatments to replace chromating for al alloys : recent developments and possible future directions 1. Russ J Non-Ferrous Met. 2012;53(2):176-203.
3. Pantelakis SG, Chamos AN, Kermanidis AT. A critical consideration for the use of Al-cladding for protecting aircraft aluminum alloy 2024 against corrosion. Theor Appl Fract Mech. 2012;57(1):36-42. http://dx.doi.org/10.1016/j.tafmec.2011.12.006.
4. Luo C, Albu SP, Zhou X, Sun Z, Zhang X, Tang Z, et al. Continuous and discontinuous localized corrosion of a 2xxx

aluminium-copper-lithium alloy in sodium chloride solution. J Alloys Compd. 2016;658:61-70.

5. Ma Y, Zhou X, Huang W, Thompson GE, Zhang X, Luo C, et al. Localized corrosion in AA2099-T83 aluminum-lithium alloy: the role of intermetallic particles. Mater Chem Phys. 2015;161:201-10.

6. Donatus U, de Viveiros BVG, de Alencar MC, Ferreira RO, Milagre MX, Costa I, et al. Correlation between corrosion resistance, anodic hydrogen evolution and microhardness in friction stir weldment of AA2198 alloy. Mater Charact. 2018;144:99-112.

7. Capelossi VR, Poelman M, Recloux I, Hernandez RPB, De Melo HG, Olivier MG. Corrosion protection of clad 2024 aluminum alloy anodized in tartaric-sulfuric acid bath and protected with hybrid sol-gel coating. Electrochim Acta. 2014;124:69-70.

8. Andreatta F, Druart M, Marin E, Cossement D, Olivier M, Fedrizzi L. Volta potential of clad AA2024 aluminium after exposure to CeCl 3 solution. Corros Sci. 2014;86:189-201. http://dx.doi.org/10.1016/j.corsci.2014.05.008.

9. Hughes AE, Scholes FH, Glenn AM, Lau D, Muster TH, Hardin SG. Factors influencing the deposition of Ce-based conversion coatings, part I: the role of Al3+ ions. Surf Coat Tech. 2009;203:2927-36. http://dx.doi.org/10.1016/j.surfcoat.2009.03.022.

10. Lau D, Glenn AM, Hughes AE, Scholes FH, Muster TH, Hardin SG. Factors influencing the deposition of Ce-based conversion coatings, Part II: the role of localised reactions. Surf Coat Tech. 2009;203:2937-45.

11. Gharbi O, Thomas S, Smith C, Birbilis N. Chromate replacement : what does the future hold ? npj Mater Degrad. 2018;2(12):23-5. http://dx.doi.org/10.1038/s41529-018-0034-5.

12. Klumpp RE, da Silva RM, Donatus U, Machado CS, Ayusso VH, Milagre MX, et al. Influência da composição da solução de tratamento de superfície na resistência à corrosão da liga aa2024-t3. Trat Superfície. 2019;212:23-8.

13. Klumpp RE. Desenvolvimento de tratamento por tecnologia limpa para a superfície da liga AA2024 com clad AA1230. [tese]. São Paulo: Instituto de Pesquisas Energéticas e Nucleares, IPEN/CNEN/SP; 2020.

14. Donatus U, Klumpp RE, Mogili NVV, Altobelli Antunes R, Milagre MX, Costa I. The effect of surface pretreatment on the corrosion behaviour of silanated AA2198-T851 Al-Cu-Li alloy. Surf Interface Anal. 2019;51(2):275-89.

15. Machado CSC, Klumpp RE, Ayusso VH, Milagre MX, Araujo JVS, Machado GAF, et al. Effect of surface treatments on the localized corrosion resistance of the AA2198 - T8 aluminum lithium alloy welded by FSW process. Surf Interface Anal. 2019;51(12):1231-9.

16. Ramé E. The interpretation of dynamic contact angles measured by the wilhelmy plate method. J Colloid Interface Sci. 1997;185:245-51. http://dx.doi.org/10.1006/jcis.1996.4589.

17. ASTM: American Society for Testing and Materials. ASTM D3359: Standard Test Methods for Rating Adhesion by Tape Test. West Conshohocken: ASTM; 2017.

18. Campestrini P, Van Westing EPM, De Wit JHW. Influence of surface preparation on performance of chromate conversion coatings on Alclad 2024 aluminium alloy Part I : nucleation and growth. Electrochim Acta. 2001;46:2553-71.

19. Schram T, de Wit JHW, Campestrini P, Terryn H, Böhm S. Study of the formation of chromate conversion coatings on Alclad 2024 aluminum alloy using spectroscopic ellipsometry. Thin Solid Films. 2002;410(1-2):76-85.

20. Simões AM, Battocchi D, Tallman DE, Bierwagen GP. SVET and SECM imaging of cathodic protection of aluminium by a Mg-rich coating. Corros Sci. 2007;49(10):3838-49.

21. Lakshmi RV, Aruna ST, Anandan C, Bera P, Sampath S. EIS and XPS studies on the self-healing properties of Ce-modified silica-alumina hybrid coatings: Evidence for Ce(III) migration. Surf Coat Tech. 2017;309:363-70.

22. Carneiro J, Tedim J, Fernandes SCM, Freire CSR, Silvestre AJD, Gandini A, et al. Chitosan-based self-healing protective coatings doped with cerium nitrate for corrosion protection of aluminum alloy 2024. Prog Org Coat. 2012;75(1-2):8-13. http://dx.doi.org/10.1016/j.porgcoat.2012.02.012.

23. Dos Santos WIA, Costa I, Tomachuk CR. Hydrothermal surface treatments with cerium and glycol molecules on the AA 2024-T3 clad alloy. Key Eng Mater. 2016;710:216-21.

24. Rosero-Navarro NC, Pellice SA, Durán A, Ceré S, Aparicio M. Corrosion protection of aluminium alloy AA2024 with cerium doped methacrylate-silica coatings. J Sol-Gel Sci Technol. 2009;52(1):31-40.

25. Child TF, Van Ooij WJ. Application of silane technology to prevent corrosion of metals and improve paint adhesion. Trans Inst Met Finish. 1999;77(2):64-70.

26. Greczynski G, Hultman LC. C 1s peak of adventitious carbon aligns to the vacuum level : dire consequences for Material ' s bonding assignment by photoelectron spectroscopy. Chemphyschem. 2017;18:1507-12.

27. Mangolini F, Mcclimon JB, Rose F, Carpick RW. Accounting for nanometer-thick adventitious carbon contamination in X ray absorption spectra of carbon-based materials. Anal Chem. 2014;86:12258-65.

28. Hinder SJ, Grilli R, Rustame M, Santos WIA, Baker MA, Costa I. A surface analytical investigation of cerium-based conversion coatings deposited onto an AA2024- T3 aluminium alloy cladding layer. Surf Interface Anal. 2014;46:735-9.

29. Hughes AE, Taylor RJ, Hinton BRW, Wilson L. XPS and SEM characterization of hydrated cerium oxide conversion coatings. Surf Interface Anal. 1995;23(7-8):540-50.

30. Sánchez-Amaya JM, Blanco G, Garcia-Garcia FJ, Bethencourt M, Botana FJ. XPS and AES analyses of cerium conversion coatings generated on AA5083 by thermal activation. Surf Coat Tech. 2012;213:105-16. http://dx.doi.org/10.1016/j.surfcoat.2012.10.027.

31. ASTM: American Society for Testing and Materials. ASTM B117: Standard Practice for Operating Salt Spray (Fog) Apparatus. West Conshohocken: ASTM; 2018.

32. He T, Zhu S. Different nanostructures of boehmite fabricated by hydrothermal process: effects of pH and anions. Cryst Eng Comm. 2009;11:1338-42.

33. Ji G, Li M, Li G, Gao G, Zou H, Gan S, et al. Hydrothermal synthesis of hierarchical micron fl ower-like γ -AlOOH and γ -Al₂O₃ superstructures from oil shale ash. Powder Technol. 2012;215-216:54-8. http://dx.doi.org/10.1016/j.powtec.2011.09.005.

34. Niroumandrad S, Rostami M, Ramezanzadeh B. Corrosion resistance of flaky aluminum pigment coated with cerium oxides/hydroxides in chloride and acidic electrolytes. Appl Surf Sci. 2015;357:2121-30. http://dx.doi.org/10.1016/j.apsusc.2015.09.195.

35. Sastri V, Bünzli J. Lanthanide complexes. In: Sastri VS, Perumareddi JR, Ramachandra Rao V, Rayudu GVS, Bunzli J-C. Modern aspects of rare earths and their complexes. Gloucester/ Ontario: Elsevier; 2003. p. 284-6.

36. Marcus Y, Abrahamer I. Anion exchange of metal complexes-VII The lanthanides-nitrate system. J Inorg Nucl Chem. 1961;22(1-2):141-50.

37. Hinton BRW, Arnot DR, Ryan NE. The corrosion inhibition of zinc with cerous chloride. Corros Sci. 1989;29(8)

38. Hugues AE, Taylor RJ, Nelson KJW, Hinton BRW, Wilson L. Characterisation of surface preparation of 2024 aluminium alloy for conversion coating. Mater Sci Technol. 1996;12(11):928-36.

39. Pinc W, Maddela S, O'Keefe M, Fahrenholtz W. Formation of subsurface crevices in aluminum alloy 2024-T3 during deposition of cerium-based conversion coatings. Surf Coat Tech. 2010;204(24):4095-100. http://dx.doi.org/10.1016/j.surfcoat.2010.05.039.